# Plasmon-resonant gold nanorods as low backscattering albedo contrast agents for optical coherence tomography

**Amy L. Oldenburg**

*Department of Electrical and Computer Engineering,*
*Beckman Institute for Advanced Science and Technology,*
*University of Illinois at Urbana-Champaign, 405 N. Mathews Ave., Urbana, IL 61801, USA*
*oldenbrg@uiuc.edu*

**Matthew N. Hansen, Daniel A. Zweifel, and Alexander Wei**

*Department of Chemistry, Purdue University, 560 Oval Dr., West Lafayette, IN 47907, USA*
*alexwei@purdue.edu*

**Stephen A. Boppart**

*Department of Electrical and Computer Engineering, Department of Bioengineering,*
*Department of Internal Medicine, Beckman Institute for Advanced Science and Technology,*
*University of Illinois at Urbana-Champaign, 405 N. Mathews Ave., Urbana, IL 61801, USA*
*boppart@uiuc.edu*

*http://biophotonics.uiuc.edu/*

**Abstract:** Plasmon-resonant gold nanorods are demonstrated as low backscattering albedo contrast agents for optical coherence tomography (OCT). We define the backscattering albedo, $a'$, as the ratio of the backscattering to extinction coefficient. Contrast agents which modify $a'$ within the host tissue phantoms are detected with greater sensitivity by the differential OCT measurement of both $a'$ and extinction. Optimum sensitivity is achieved by maximizing the difference between contrast agents and tissue, $|a'_{ca} - a'_{tiss}|$. Low backscattering albedo gold nanorods ($14 \times 44$ nm; $\lambda_{max} = 780$ nm) within a high backscattering albedo tissue phantom with an uncertainty in concentration of 20% (randomized $2\pm0.4\%$ intralipid) were readily detected at 82 ppm (by weight) in a regime where extinction alone could not discriminate nanorods. The estimated threshold of detection was 30 ppm.

© 2006 Optical Society of America

**OCIS codes:** (170.4500) Optical coherence tomography; (170.3880) Medical and biological imaging; (290.5850) Scattering, particles.

## References and links

1. D. Huang, E. A. Swanson, C. P. Lin, J. S. Schuman, W. G. Stinson, W. Chang, M. R. Hee, T. Flotte, K. Gregory, C. A. Puliafito, and J. G. Fujimoto, "Optical coherence tomography," Science **254**, 1178–1181 (1991).
2. S. A. Boppart, A. L. Oldenburg, C. Xu, and D. L. Marks, "Optical probes and techniques for molecular contrast enhancement in coherence imaging," J. Biomed. Opt. **10**, 041208–1–14 (2005).
3. U. Morgner, W. Drexler, F. X. Kartner, X. D. Li, C. Pitris, E. P. Ippen, and J. G. Fujimoto, "Spectroscopic optical coherence tomography," Opt. Lett. **25**, 111–113 (2000).
4. J. F. de Boer, T. E. Milner, M. J. C. van Gemert, and J. S. Nelson, "Two-dimensional birefringence imaging in biological tissue by polarization-sensitive optical coherence tomography," Opt. Lett. **22**, 934–936 (1997).

5. K. D. Rao, M. A. Choma, S. Yazdanfar, A. M. Rollins, and J. A. Izatt, "Molecular contrast in optical coherence tomography by use of a pump-probe technique," Opt. Lett. **28**, 340–341 (2003).

6. D. L. Marks and S. A. Boppart, "Nonlinear interferometric vibrational imaging," Phys. Rev. Lett. **92**, 123905–1–4 (2004).

7. J. K. Barton, J. B. Hoying, and C. J. Sullivan, "Use of microbubbles as an optical coherence tomography contrast agent," Acad. Radiol. **9**, S52–S55 (2002).

8. T. M. Lee, A. L. Oldenburg, S. Sitafalwalla, D. L. Marks, W. Luo, F. J.-J. Toublan, K. S. Suslick, and S. A. Boppart, "Engineered microsphere contrast agents for optical coherence tomography," Opt. Lett. **28**, 1546–1548 (2003).

9. C. Xu, D. L. Marks, and S. A. Boppart, "Near-infrared dyes as contrast-enhancing agents for spectroscopic optical coherence tomography," Opt. Lett. **29**, 1647–1649 (2004).

10. C. Yang, L. E. L. McGuckin, J. D. Simon, M. A. Choma, B. E. Applegate, and J. A. Izatt, "Spectral triangulation molecular contrast optical coherence tomography with indocyanine green as the contrast agent," Opt. Lett. **29**, 2016–2018 (2004).

11. A. L. Oldenburg, F. J.-J. Toublan, K. S. Suslick, A. Wei, and S. A. Boppart, "Magnetomotive contrast for *in vivo* optical coherence tomography," Opt. Express **13**, 6597–6614 (2005). http://www.opticsexpress.org/abstract.cfm?id=85327.

12. Y. Zhao, B. Sadtler, M. Lin, G. H. Hockerman, and A. Wei, "Nanoprobe implantation into mammalian cells by cationic transfection," Chem. Commun. pp. 784–785 (2004).

13. E. E. Connor, J. Mwamuka, A. Gole, C. J. Murphy, and M. D. Wyatt, "Gold nanoparticles are taken up by human cells but do not cause acute cytotoxicity," Small **1**, 325–327 (2005).

14. H. Takahashi, Y. Niidome, T. Niidome, K. Kaneko, H. Kawasaki, and S. Yamada, "Modification of gold nanorods using phosphatidylcholine to reduce cytotoxicity," Langmuir **22**, 2–5 (2006).

15. S. J. Oldenburg, R. D. Averitt, S. L. Westcott, and N. J. Halas, "Nanoengineering of optical resonances," Chem. Phys. Lett. **288**, 243–247 (1998).

16. C. Loo, A. Lin, L. Hirsch, M.-H. Lee, J. Barton, N. Halas, J. West, and R. Drezek, "Nanoshell-enabled photonics-based imaging and therapy of cancer," Technol. Cancer Res. Treat. **3**, 33–40 (2004).

17. J. Chen, B. Wiley, Z.-Y. Li, D. Campbell, F. Saeki, H. Cang, L. Au, J. Lee, X. Li, and Y. Xia, "Gold nanocages: engineering their structure for biomedical applications," Adv. Mater. **17**, 2255–2261 (2005).

18. K. Chen, Y. Liu, G. Ameer, and V. Backman, "Optimal design of structured nanospheres for ultrasharp light-scattering resonances as molecular imaging multilabels," J. Biomed. Opt. **10**, 024005–1–6 (2005).

19. H. Cang, T. Sun, Z.-Y. Li, J. Chen, B. J. Wiley, Y. Xia, and X. Li, "Gold nanocages as contrast agents for spectroscopic optical coherence tomography," Opt. Lett. **30**, 3048–3050 (2005).

20. J. Yguerabide and E. E. Yguerabide, "Light-scattering submicroscopic particles as highly fluorescent analogs and their use as tracer labels in clinical and biological applications," Anal. Biochem. **262**, 137–156 (1998).

21. S. Link, M. B. Mohamed, and M. A. El-Sayed, "Simulation of the optical absorption spectra of gold nanorods as a function of their aspect ratio and the effect of the medium dielectric constant," J. Phys. Chem. B **103**, 3073–3077 (1999).

22. C. Burda, X. Chen, R. Narayanan, and M. A. El-Sayed, "Chemistry and properties of nanocrystals of different shapes," Chem. Rev. **105**, 1025–1102 (2005).

23. J. Perez-Juste, I. Pastoriza-Santos, L. M. Liz-Marzan, and P. Mulvaney, "Gold nanorods: Synthesis, characterization and applicatons," Coord. Chem. Rev. **249**, 1870–1901 (2005).

24. H. Wang, T. B. Huff, D. A. Zweifel, W. He, P. S. Low, A. Wei, and J.-X. Cheng, "*In vitro* and *in vivo* two-photon luminescence imaging of single gold nanorods," Proc. Natl. Acad. Sci. USA **102**, 15752–15756 (2005).

25. C. Sonnichsen, T. Franzl, T. Wilk, G. von Plessen, J. Feldmann, O. Wilson, and P. Mulvaney, "Drastic reduction of plasmon damping in gold nanorods," Phys. Rev. Lett. **88**, 077402–1–4 (2002).

26. C. F. Bohren and D. R. Huffman, *Absorption and Scattering of Light by Small Particles*, pp. 141–154 (John Wiley and Sons, 1983).

27. A. I. Kholodnykh, I. Y. Petrova, K. V. Larin, M. Motamedi, and R. O. Esenaliev, "Precision of measurement of tissue optical properties with optical coherence tomography," Appl. Opt. **42**, 3027–3037 (2003).

28. D. Levitz, L. Thrane, M. H. Frosz, P. E. Andersen, C. B. Andersen, J. Valanciunaite, J. Swartling, S. Andersson-Engels, and P. R. Hansen, "Determination of optical scattering properties of highly-scattering media in optical coherence tomography images," Opt. Express **12**, 249–259 (2004). http://www.opticsexpress.org/abstract.cfm?id=78584.

29. L. Thrane, M. H. Frosz, T. M. Jorgensen, A. Tycho, H. T. Yura, and P. E. Andersen, "Extraction of optical scattering parameters and attenuation compensation in optical coherence tomography images of multilayered tissue structures," Opt. Lett. **29**, 1641–1643 (2004).

30. D. J. Faber, F. J. van der Meer, and M. C. G. Aalders, "Quantitative measurement of attenuation coefficients of weakly scattering media using optical coherence tomography," Opt. Express **12**, 4353–4365 (2004). http://www.opticsexpress.org/abstract.cfm?id=81159.

31. J. M. Schmitt, A. Knuttel, and R. F. Bonner, "Measurement of optical properties of biological tissues by low-coherence reflectometry," Appl. Opt. **32**, 6032–6042 (1993).

32. W.-F. Cheong, S. A. Prahl, and A. J. Welch, "A review of the optical properties of biological tissues," IEEE J. Quantum Electron. **26**, 2166–2185 (1990).
33. T. L. Troy and S. N. Thennadil, "Optical properties of human skin in the near infrared wavelength range of 1000 to 2200 nm," J. Biomed. Opt. **6**, 167–176 (2001).
34. J. W. Pickering, S. A. Prahl, N. van Wieringer, J. F. Beek, H. J. C. M. Sterenborg, and M. J. C. van Gemert, "Double-integrating-sphere system for measuring the optical properties of tissue," Appl. Opt. **32**, 399–410 (1993).
35. A. L. Oldenburg, D. A. Zweifel, C. Xu, A. Wei, and S. A. Boppart, "Characterization of plasmon-resonant gold nanorods as near-infrared optical contrast agents investigated using a double-integrating sphere system," in *Proceedings of SPIE: Plasmonics in biology and medicine II*, vol. 5703, pp. 50–60 (2005).
36. G. Zaccanti, S. D. Bianco, and F. Marelli, "Measurements of optical properties of high-density media," Appl. Opt. **42**, 4023–4030 (2003).
37. T. G. van Leeuwen, D. J. Faber, and M. C. Aalders, "Measurement of the axial point spread function in scattering media using single-mode fiber-based optical coherence tomography," IEEE J. Sel. Top. Quantum Electron. **9**, 227–233 (2003).
38. W. H. Press, B. P. Flannery, S. A. Teukolsky, and W. T. Vetterling, *Numerical Recipes in Pascal*, pp. 572–574 (Cambridge University Press, 1989).
39. D. A. Zweifel and A. Wei, "Sulfide-arrested growth of gold nanorods," Chem. Mater. **17**, 4256–4261 (2005).
40. A. Nel, T. Xia, L. Madler, and N. Li, "Toxic potential of materials at the nanolevel," Science **311**, 622–627 (2006).
41. J. M. Schmitt, A. Knuttel, M. Yadlowsky, and M. A. Eckhaus, "Optical-coherence tomography of a dense tissue: statistics of attenuation and backscattering," Phys. Med. Biol. **39**, 1705–1720 (1994).
42. M. Liu and P. Guyot-Sionnest, "Mechanism of silver(I)-assisted growth of gold nanorods and bipyramids," J. Phys. Chem. B **109**, 22192–22200 (2005).
43. B. Hermann, K. Bizheva, A. Unterhuber, B. Povazay, H. Sattmann, L. Schmetterer, A. F. Fercher, and W. Drexler, "Precision of extracting absorption profiles from weakly scattering media with spectrosocpic time-domain optical coherence tomography," Opt. Express **12**, 1677–1688 (2004). http://www.opticsexpress.org/abstract.cfm?id=79601.
44. C.-H. Chou, C.-D. Chen, and C. R. C. Wang, "Highly efficient, wavelength-tunable, gold nanoparitcle based optothermal nanoconvertors," J. Phys. Chem. B **109**, 11135–11138 (2005).
45. L. R. Hirsch, R. J. Stafford, J. A. Bankson, S. R. Sershen, B. Rivera, R. E. Price, J. D. Hazle, N. J. Halas, and J. L. West, "Nanoshell-mediated near-infrared thermal therapy of tumors under magnetic resonance guidance," Proc. Natl. Acad. Sci. USA **100**, 13549–13554 (2003).
46. X. Huang, I. H. El-Sayed, W. Qian, and M. A. El-Sayed, "Cancer cell imaging and photothermal therapy in the near-infrared region by using gold nanorods," J. Am. Chem. Soc. **128**, 2115–2120 (2006).
47. T. B. Huff, M. H. Hansen, Y. Zhao, J.-X. Cheng, and A. Wei, "CTAB-mediated cell uptake of gold nanorods," Manuscript submitted (2006).
48. H. Liao and J. H. Hafner, "Gold nanorod bioconjugates," Chem. Mater. **17**, 4636–4641 (2005).
49. Y. Zhao, W. Perez-Segarra, Q. Shi, and A. Wei, "Dithiocarbamate assembly on gold," J. Am. Chem. Soc. **127**, 7328–7329 (2005).

## 1. Introduction

Optical coherence tomography (OCT) is a non-invasive biomedical imaging modality which provides real-time, depth-resolved structural and functional images typically a few millimeters deep into biological tissue.[1] There has been much interest in developing mechanisms for molecular imaging with OCT, as it would significantly extend its diagnostic capabilities.[2] Various OCT modalities such as spectroscopic OCT,[3] polarization-sensitive OCT,[4] pump-probe OCT,[5] and nonlinear interferometric vibrational imaging[6] have provided chemically-specific (molecular) imaging of specific classes of endogenous biomolecules. The introduction of exogenous contrast agents targeted to a broader class of biomolecules in tissue increases the versatility of molecular OCT imaging, analogous to histological stains.[2] However, because OCT is a coherence imaging technique, it is inherently blind to fluorescent or bioluminescent probes. Therefore, the development of alternative probes and associated OCT imaging techniques has recently become an active area of investigation. Examples of OCT contrast agents include highly scattering microbubbles[7] and microspheres[8] with the potential to carry therapeutic agents, near-infrared (NIR) absorbing dyes for detection with spectroscopic OCT,[9, 10] and magnetic nanoparticles which provide contrast in OCT via induced motion under external

magnetic field modulation.[11] To date, these strategies have been employed with varying degrees of success, yet OCT imaging of site-directed contrast agents with high sensitivity, specificity, resolution, and depth penetration have not been demonstrated in a living organism.[2]

Gold nanoparticles have excellent potential as OCT contrast agents, because they have a low intrinsic cytotoxicity [12, 13, 14] and can be engineered to support localized surface plasmon resonances (SPRs) at NIR wavelengths. Recent examples of engineered particles include gold nanoshells grown on submicron silica cores, whose resonance can be tuned as a function of core-shell aspect ratio[15, 16], and hollow, cube-like gold nanocages whose plasmon resonances can be modulated by adjusting their porosity.[17] There are several criteria to consider when designing plasmon-resonant nanoparticles as biomedical contrast agents, in addition to a large NIR optical cross section. Small particle sizes (typically $< 100$ nm) are desired to permit extravasation from the blood pool and increase tissue transport, and sharp spectral linewidths are important for enhancing contrast by spectroscopic OCT (SOCT).[18, 19] By these criteria, the use of anisotropic nanoparticles is more desirable than submicron ($> 100$ nm) spherical gold particles[20] or nanoshells,[16] whose NIR responses are spectrally broad (FWHM $> 200$ nm).

Gold nanorods are especially appealing because they can be synthesized with dimensions well below 100 nm, and their longitudinal plasmon resonances are readily tuned to NIR frequencies used in OCT imaging by adjusting their aspect ratio (length/width).[21, 22, 23]. Nanorods exhibit highly anisotropic absorption which depends on the orientation of the long axis of the rod,[24] which might be exploited using polarization-sensitive OCT techniques. The absorption cross section of nanorods per unit particle volume (averaged over all orientations) is comparable to that of other types of plasmon-resonant nanoparticles. However, with respect to the quality of optical response, the half-maximum linewidths of single gold nanorods can be as narrow as 0.1 eV ($\Gamma \sim 50$ nm at $\lambda_{max} = 800$ nm) due to their low rates of plasmon decay.[25]

Plasmon-resonant nanoparticles and nanorods have a size-dependent albedo (ratio of scattering to total extinction), because their absorption cross sections scale linearly with particle volume, whereas their scattering cross sections scale as the square of the volume.[26] A fundamental question we explore here is whether the choice of albedo affects the sensitivity of detection with OCT. Primarily, the depth-dependent OCT signal is dictated by the tissue optical backscattering and extinction coefficients, $\mu_b$ and $\mu_t$. Thus $\mu_t$ is measured from the exponential decay of the OCT signal over depth, and $\mu_b$ is measured from the overall amplitude. Previous work shows that $\mu_t$ is extracted by measuring attenuation in the depth-dependent OCT signal,[27, 28, 29, 30] and the contribution of multiple-scattering also depends on $g$, the average cosine of the scattering angle.[28, 29] The definition of $\mu_b$ used here has been given previously as the 180 degree scattering coefficient,[31] which determines the light power collected from the sample in the OCT imaging geometry. Given sufficient speckle-averaging, it is possible to measure $\mu_b$ from the OCT signal amplitude, with demonstrated precisions of 0.7% in human skin.[27]

The sensitivity of contrast agent detection by OCT depends on the relative change in $\mu_b$ and $\mu_t$ within tissue by the contrast agents. Many previous studies have focused solely on changes in $\mu_t$ in a tissue phantom after the addition of contrast agents;[8, 19] however, in a heterogeneous medium with variable values of $\mu_t$, the amount of contrast agents needed to modify $\mu_t$ above this level of uncertainty can be prohibitive. Other detection modes are based purely on extinction, but these neglect the contribution of $\mu_b$ and thus cannot distinguish between primarily absorbing- or scattering-based mechanisms.

We recognize that the measurement of $\mu_b$ allows for extraction of a dimensionless parameter $a' = \mu_b/\mu_t$, a type of albedo which only depends on the cross sections of the scatterers.[31] This parameter, dubbed backscattering albedo, is an under appreciated but practical metric for

generating optical contrast. Here we show that the backscattering albedo offers significant benefits for enhancing OCT detection of contrast agents situated within a tissue-like medium. We demonstrate theoretically and experimentally that the measurement of $a'$ increases the sensitivity of OCT contrast agents. In addition, we find low backscattering albedo gold nanorods to be particularly well-suited for modifying $a'$ in biological tissues, which typically are dominated by forward-scattering.[32] The addition of nanorods to tissue decreases $a'$ while increasing $\mu_t$, which we verified by imaging gold nanorods in tissue phantoms of 2% intralipid.[33] Higher backscattering albedo silica spheres were investigated as a comparison, to demonstrate the relative merits of scattering- versus absorption-based contrast. The detectability of nanorods and silica spheres by OCT were correlated with their bulk optical properties characterized by a double-integrating sphere system[34], which established the most important qualities in the design of OCT contrast agents.

## 2. Theory

### 2.1. Molecular contrast imaging method

The primary goal of molecular imaging is to garner information of biological relevance beyond the structural information provided with OCT images. Contrast agents may be designed as blood pool agents to collect in regions of "leaky vasculature", for example, or they may be biochemically targeted to a specific cell surface receptor or chemical event. To achieve the goal of obtaining concentration maps of the contrast agents within an OCT image, one must optimize the sensitivity and specificity of the imaging modality for these agents, as well as the chemical specificity of the agents to the molecular target. (Imaging specificity has been investigated in an earlier study.[35]) In this work we improve sensitivity (*i.e.*, sensitivity of the imaging system to the contrast agent) by fitting the backscattering and extinction coefficients of the medium to the depth-dependent OCT profile. The addition of contrast agents modifies these parameters, allowing for extraction of their concentration. However, this method, like the previous method using only extinction, requires prior knowledge of the optical properties of both the tissue and the contrast agent. In practice this means that baseline OCT images of the tissue of interest, or of an ensemble of similar tissues in a large number of patients, must be obtained *a priori*. For simplicity we assume homogeneous tissue where the depth-dependent response is averaged over uncorrelated speckles (either by temporal or spatial averaging).[27] In future work this analysis could be extended to account for structures with multiple layers.[29, 30]

In the independent scattering approximation,(*e.g.*,[36]), one can write the backscattering and extinction coefficients of the medium ($\mu_b$ and $\mu_t$, respectively) as a linear combination of the optical properties of endogenous tissue and exogenous contrast agents:

$$\mu_b = \varepsilon_{b,tiss}\tilde{\rho}_{tiss} + \varepsilon_{b,ca}\rho_{ca} \qquad (1)$$
$$\mu_t = \varepsilon_{t,tiss}\tilde{\rho}_{tiss} + \varepsilon_{t,ca}\rho_{ca}$$

where $\varepsilon_{b,ca}$ and $\varepsilon_{t,ca}$ are the molar backscattering and extinction coefficients of the contrast agent, respectively, and $\rho_{ca}$ is the unknown concentration of contrast agents. The contribution of the tissue optical properties can be expressed in terms of an effective concentration $\tilde{\rho}_{tiss}$ which is a random variable with a mean $<\tilde{\rho}_{tiss}>$ and standard deviation $\sigma_{\tilde{\rho}_{tiss}}$ determined by prior measurements. In practice we set $<\tilde{\rho}_{tiss}>= 1$, assign the molar coefficients $\varepsilon_{s,tiss}$ and $\varepsilon_{t,tiss}$ as the backscattering and extinction coefficients of the tissue respectively, and report $\sigma_{\tilde{\rho}_{tiss}}$ as a fractional error in the measured tissue coefficients. It should be noted that the fluctuations observed in tissue are assumed to arise from changes in scatterer density, and not changes in the type of scatterer (which modify $a'$ and might confound the detection of contrast agents). However, it is an intriguing future possibility that this method might be used to differentiate endogenous scatterer types.

Solving Eq.(1) for the contrast agent concentration $\rho_{ca}$ gives:

$$\rho_{ca} = \frac{\mu_b \varepsilon_{t,tiss} - \mu_t \varepsilon_{b,tiss}}{\varepsilon_{b,ca} \varepsilon_{t,tiss} - \varepsilon_{t,ca} \varepsilon_{b,tiss}} = \frac{\mu_t (a'_{med} - a'_{tiss})}{\varepsilon_{t,ca}(a'_{ca} - a'_{tiss})} \qquad (2)$$

where the backscattering albedo is defined for the medium as $a'_{med} = \mu_b/\mu_t$, for tissue as $a'_{tiss} = \varepsilon_{b,tiss}/\varepsilon_{t,tiss}$, and for contrast agents as $a'_{ca} = \varepsilon_{b,ca}/\varepsilon_{t,ca}$. Note that $\rho_{ca}$ is undefined when $a'_{ca} = a'_{tiss}$, because the linear system of Eq. (1) becomes underdetermined. This can be appreciated intuitively: when the contrast agents have the same $a'$ as the tissue, it becomes impossible to distinguish tissue fluctuations from the presence or absence of the agents. Only when the backscattering albedo of the tissue is modified by the contrast agents can this ambiguity be resolved. Therefore, in the limit of $a'_{ca} = a'_{tiss}$ only the prior information about the tissue extinction can be used to solve for $\rho_{ca}$:

$$\rho_{ca} = \frac{\mu_t - \varepsilon_{t,tiss} < \tilde{\rho}_{tiss} >}{\varepsilon_{t,ca}} \qquad \text{for } a'_{ca} = a'_{tiss} \qquad (3)$$

which is essentially the same as the extinction-based method used in previous works.[19]

The goal here is to minimize the uncertainty $\sigma_{\rho_{ca}}$ in the measurement of $\rho_{ca}$. In the former case ($a'_{ca} \neq a'_{tiss}$), it depends on the accuracy of the fit of $\mu_b$ and $\mu_t$ to the OCT data, and ultimately on the noise of the OCT system $\sigma_{OCT}$. Assuming this noise is independent of the addition of contrast agents, $\sigma_{\rho_{ca}}$ decreases as the difference between the contrast agent and tissue backscattering albedos are increased. However, in the limiting case $a'_{ca} = a'_{tiss}$, the uncertainty is typically dominated by $\sigma_{\tilde{\rho}_{tiss}}$. In most practical cases, solving for $\rho_{ca}$ by fitting both $\mu_b$ and $\mu_t$ to the OCT data and using Eq.(2) is more accurate than fitting just $\mu_t$ and using Eq.(3). Based on Eqs.(2) and (3) and assuming Gaussian statistics we derive the following:

$$\sigma_{\rho_{ca}} \propto \frac{\sigma_{OCT}}{|a'_{ca} - a'_{tiss}|} \qquad \text{for } a'_{ca} \neq a'_{tiss} \qquad (4)$$

$$\sigma_{\rho_{ca}} \approx \frac{\varepsilon_{t,tiss}}{\varepsilon_{t,ca}} \sigma_{\tilde{\rho}_{tiss}} \qquad \text{for } a'_{ca} = a'_{tiss} \qquad (5)$$

Equations (4) and (5) show analytically how the sensitivity of the contrast agent measurement depends on the $a'$ of the contrast agents, variance in the tissue optical properties, and noise in the OCT imaging hardware. In the following subsection we validate these concepts by simulating a realistic imaging scenario.

## 2.2. Sensitivity analysis via Monte Carlo simulations

Eqs.(4) and (5) predict the error $\sigma_{\rho_{ca}}$, which is essentially the minimum detectable concentration of contrast agents, (or equivalently sensitivity to contrast agents) for a unity signal-to-noise ratio (SNR=1). To prove that the above technique is useful for a typical imaging scenario, we simulate the process of OCT imaging exhibiting shot noise and tissue fluctuations. Then $\rho_{ca}$ is fit to the depth-dependent OCT data given prior knowledge of $\tilde{\rho}_{tiss}$. This is performed a large number of times using a set of random tissues to estimate the deviations $\rho_{ca}$.

The depth-dependent OCT signal $S_{OCT}$ (demodulated photocurrent) is proportional to the electric field strength scattered from the medium at depth $z$ below the surface of the homogeneous medium. In the single-scattering approximation this can be written:

$$S_{OCT}(z) = S_0 \sqrt{\mu_b(\tilde{\rho}_{tiss}, \rho_{ca})} \exp(-\mu_t(\tilde{\rho}_{tiss}, \rho_{ca})z) f(z - z_f, z_R) \qquad (6)$$

where $S_0$ is a system hardware parameter determined by the sensitivity of the OCT system and $f$ accounts for the loss of efficiency away from the focus at depth $z_f$. For single-mode fiber-based OCT systems $f$ is the square root of a Lorentzian with Rayleigh range $z_R$.[37] In this

simulation we use this form of $f$, and presume that $z_f$ and $z_R$ are known from calibration of the system.

OCT data sets of $N = 1000$ equally spaced points $(z = 0...z_{max})$ were computed via Eq. (6) using randomized $\tilde{\rho}_{tiss}$ from a Gaussian distribution with $< \tilde{\rho}_{tiss} >$ and $\sigma_{\rho_{tiss}}$, which are the priors. Shot noise was simulated by adding Gaussian random noise to each point $S_i$ with zero mean and deviation $\sigma_{OCT}$. Least-squares fitting of the simulated data to fit the parameters $\tilde{\rho}_{tiss}$ and $\rho_{ca}$ were subsequently performed using Eq.(6). In order to use the priors to aid in the fitting procedure, the least-squares parameter $\chi^2$ was defined in the following way:

$$\chi^2 = \sum_{i=1}^{N} \left( \frac{S_i - S_{OCT}(\tilde{\rho}_{tiss}, \rho_{ca})}{\sigma_{OCT}} \right)^2 + \left( \frac{\tilde{\rho}_{tiss} - < \tilde{\rho}_{tiss} >}{\sigma_{\tilde{\rho}_{tiss}}} \right)^2 \qquad (7)$$

Using initial parameters $\rho_{ca} = 0$ and $\tilde{\rho}_{tiss} = < \tilde{\rho}_{tiss} >$, the inverse Hessian method[38] was used to iteratively minimize $\chi^2$. A typical data set and best-fit line plotted in Fig. 1a illustrate the efficacy of this least-squares technique. Unless otherwise noted, the parameter values used were: $S_0 = 1$ mm$^{1/2}$, $\sigma_{OCT} = 10^{-2}$ mm$^{1/2}$, $< \tilde{\rho}_{tiss} > = 1$, $\sigma_{\tilde{\rho}_{tiss}} = 0.1$, $\varepsilon_{t,tiss} = \varepsilon_{t,ca} = 4$ mm$^{-1}$, $a'_{tiss} = 0.9$, $a'_{ca} = 0.5$, $z_{max} = 2$ mm, $z_R = 0.4$ mm, $z_f = 0.6$ mm, and $\rho_{ca} = 0.1$ which was blind to the fitting procedure. (For ease of discussion $\sigma_{OCT}$ will subsequently be reported as a unitless parameter that is a fraction of $S_0$. We also note that the parameter $a'$ is in general a number $\ll 1$, numbers close to 1 were chosen for simplicity. The absolute scaling of $a'$ does not affect the following conclusions). The detection error $\sigma_{\rho_{ca}}$, assuming a Gaussian distribution, was determined by measuring the 68% confidence interval. A typical measurement comprising $n = 1000$ simulations is illustrated in Fig. 1b.
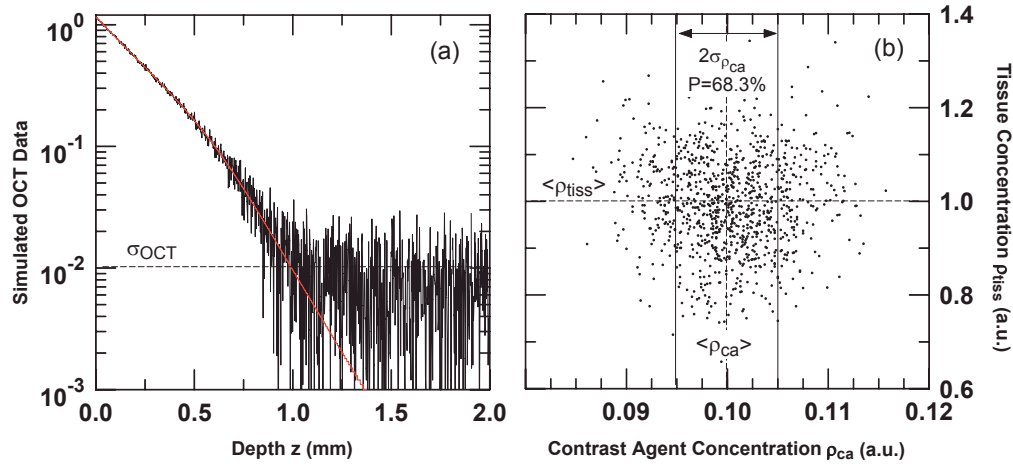


Fig. 1. Monte Carlo simulations of contrast agent detection with OCT. (a) Example depth-dependent OCT data with added shot noise (black) and corresponding least-squares line (red) fit to Eq.(6). (b) Scatter plot of the best fit values of $\tilde{\rho}_{tiss}$ and $\rho_{ca}$ for 1000 independent experiments. The value of $\sigma_{\rho_{ca}}$ is taken to be half the 68% confidence interval.

Additional Monte Carlo simulations ($n = 1000$) were performed to measure $\sigma_{\rho_{ca}}$ via the above procedure while varying $a'_{ca}$ and keeping $\varepsilon_{t,ca}$ and all other parameters fixed. We find

empirically that the resulting curves fit the square root of a Lorentzian:

$$\sigma_{\rho_{ca}}(a'_{ca}) = \sigma_0 \left( \left( \frac{a'_{ca} - a'_{tiss}}{\Delta a'} \right)^2 + 1 \right)^{-1/2} \tag{8}$$

$$\approx \frac{\sigma_0 \Delta a'}{|a'_{ca} - a'_{tiss}|} \qquad \text{for } |a'_{ca} - a'_{tiss}| \gg \Delta a' \tag{9}$$

where $\Delta a'$ and $\sigma_0$ are fit parameters indicative of the curve width and height, respectively. Results of these simulations for varying values of shot noise and tissue fluctuations are shown in Fig. 2.
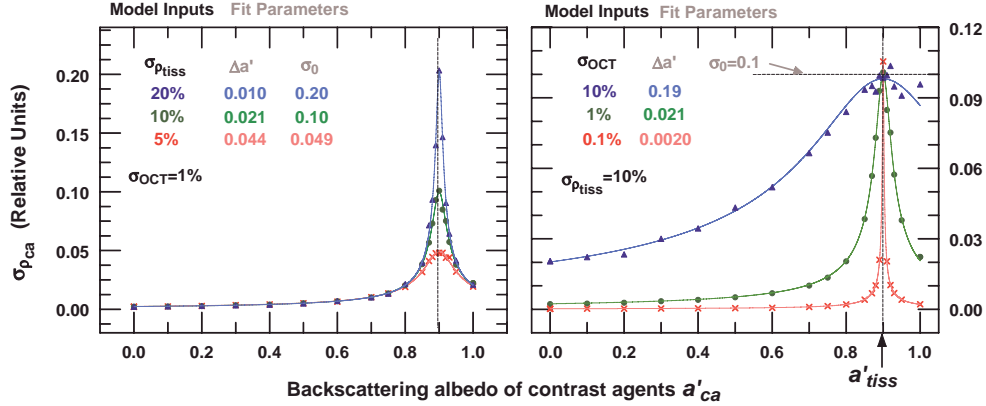


Fig. 2. Plots of uncertainty in measurement of contrast agent concentration $\sigma_{\rho_{ca}}$ versus backscattering albedo $a'_{ca}$. Results of Monte Carlo simulations (points) are plotted with their best-fit line according to Eq.(8) with fit parameters $\sigma_0$ and $\Delta a'$. The left plot shows results obtained while varying the degree of tissue fluctuations, and the right plot illustrates varying levels of OCT shot noise. All other parameters are specified in the text.

Two observations are immediately apparent from Fig. 2. First, the maximum in $\sigma_{\rho_{ca}}$, which equals $\sigma_0$, occurs when $a'_{ca} = a'_{tiss}$. It scales proportionally with the tissue fluctuations but is uncorrelated with the OCT shot noise, and its numerical values are in excellent agreement with Eq.(5). These errors are essentially the same as those obtained from curve fits based on extinction alone. Second, the error for contrast agent $a'$ far from that of the tissue is dependent on the OCT shot noise but not tissue fluctuations, as predicted in Eq.(4). By comparing Eq.(4) with Eq.(9) we see that the curve width $\Delta a'$ should be $\propto \sigma_{OCT}/\sigma_{\rho_{tiss}}$, which is confirmed by the findings in Fig. 2.

The implications of these results is that the sensitivity of detection can be improved considerably by choice of a contrast agent whose backscattering albedo is significantly different from the tissue, given a fixed contrast agent molar extinction. Optimum sensitivity is achieved by maximizing the difference $|a'_{ca} - a'_{tiss}|$. For the imaging system and tissue phantoms in the experiments to follow we found that $\sigma_{OCT}$ was typically between 1-10%, suggesting that careful choice of $a'_{ca}$ is important in the presence of tissue fluctuations. The difference between $a'_{ca}$ and $a'_{tiss}$ needed to significantly improve the sensitivity is described by the $1/\sqrt{2}$ half linewidth $\Delta a'$, which appears to be small ($< 0.1$) in most of the examples here. However, for differences much larger than $\Delta a'$, the improvement in sensitivity becomes inversely proportional to the difference, according to Eq. (9).

In the experiments below, we examine nanorods and silica spheres with $a'$ that are one tenth and one half that of the tissue phantom, respectively. Based on the simulations in Fig. 2, the

low backscattering albedo nanorods are anticipated to have at most half the minimum detectible concentration as the higher backscattering albedo silica spheres, given the same amount of extinction.

## 3. Experimental methods

### 3.1. Nanorod synthesis and optical characterization

Gold nanorods were synthesized using a seeded growth method and treated with sodium sulfide to prevent a shift in their optical resonances over time.[39] Briefly, $AuCl_4$ was reduced onto gold seeds ($\sim$3.5 nm) in the presence of the micelle-forming surfactant cetyltrimethylammonium bromide. The nanorods were treated with $Na_2S$, then centrifuged and resuspended in deionized water. Nanorod size analysis ($n = 1908$) was performed using transmission electron microscopy (TEM, Philips CM200, FEI Company). Gold concentration was measured using inductively-coupled plasma mass spectrometry (OES Optima 2000 DV, Perkin Elmer). The nanorod extinction spectrum was measured with a spectrophotometer (USB-ISS-VIS, Ocean Optics, Inc.). The nanorod diffuse optical properties were measured using a customized double-integrating sphere (DIS) system described in detail elsewhere.[35] Briefly, two integrating spheres 100 mm diameter (Zenith coating, SphereOptics-Hoffman, LLC) fitted with Si photodetectors collected the diffuse reflectance and diffuse transmittance from an intervening liquid sample in a 210 $\mu$m thick cell. Collimated light from a laser diode at 768 nm was incident upon the sample, and the collimated transmission was measured using a power meter $>$ 1 m from the sample (Coherent Field Master GS). The inverse-adding-doubling algorithm (IAD v.1.6 by S. Prahl) was employed to obtain the optical scattering, extinction, and anisotropy factors $\mu_s$, $\mu_t$, and $g$, respectively, based on the photodetector measurements. Because DIS measurements are most accurate when the albedo is between 0.4 and 0.95,[34] the nanorod albedo was extracted by measuring various mixtures of nanorods with Liposyn™ ($n = 23$, 0-68 ppm nanorods, 0.5-1% Liposyn II, Abbott Labs, diluted from 10%). The pure nanorod solution did not exhibit sufficient scattering to obtain $g$. Pure solutions of the 2% Intralipid™ tissue phantom (diluted from 10%, Fresenius Kabi, Sweden) and solutions of 800 nm silica spheres (SS03N, Bangs Labs) both pure (for measurement of $g$) and mixed with intralipid were also characterized using the DIS system. All solutions were diluted with deionized water as needed. A comparison of measured $\mu_t$ values with those predicted by Eq.(1) was performed to confirm the validity of the independent scattering approximation for each mixture.

### 3.2. Tissue phantom OCT imaging

The single-mode, fiber-based, time-domain OCT system centered at 800 nm used here has been described in detail elsewhere.[11] Briefly, imaging light with a bandwidth of 110 nm was provided by a Ti:Sapphire laser (KMLabs, Inc.), with $\sim$ 10 mW of power at the sample. A 40 mm focal length imaging lens was used. The in-focus resolution was 3 $\mu$m axial and 8 $\mu$m transverse. Optical delay was provided by an oscillating retroreflector at 10 Hz. Dual-balanced detection was used (New Focus Nirvana), and digital bandpass filtering was employed to increase the system sensitivity to -100 dB. Liquid samples were imaged in M-mode with an optical depth of 2 mm, acquiring 600 pixels transverse and 1000 pixels axial for each image. We found that at a rate of 10 Hz there was sufficient speckle-decorrelation between scans in these aqueous solutions to avoid the need for B-mode imaging. A coverslip was placed atop each liquid sample to prevent strong surface reflections. At the beginning of each imaging session, images of 0.5% and 2% intralipid were acquired to calibrate the focusing parameters ($z_R$, $z_f$) and absolute system sensitivity parameter $S_0$, respectively. Also, the images of 2% intralipid were used as tissue priors from which the initial $a'$ of the tissue was calibrated.

To determine the stability of the measurement of $a'$ over varying $\rho_{tiss}$, intralipid solutions of varying concentration (0.0078% to 2%, $n = 13$) were imaged. The dose-dependent response was then investigated by mixing either nanorods (0 to 110 ppm, $n = 8$) or silica spheres (0 to 0.84% v/v, $n = 9$) with a fixed intralipid concentration of 2%, and acquiring OCT images. The ability to detect contrast agents within a fluctuating medium was investigated by preparing intralipid according to a computer-generated list of Gaussian random concentrations with a mean of 2% and deviation of 0.4% (or 20% of the mean). A set of 10 random solutions were imaged, where 5 contained nanorods (82 ppm) and 5 were controls. For all experiments described above, the chronological order in which solution sets were imaged was randomized.

### 3.3.  Image analysis

OCT images were analyzed according to the following sequence. For each image, the top surface was identified, and the data points above the surface were averaged to estimate the shot noise $\sigma_{shot}$. The 600 columns in each image were then partitioned into 12 subgroups for independent analysis. The depth-dependent signal for each subgroup was computed by averaging across the rows, then subtracting by and subsequently dividing by $\sigma_{shot}$, to provide an SNR-based signal that approaches 0 for large depths. Nonlinear least-squares fits were performed while weighting each point $S_i$ by $1/(S_i+1)$ to approximate the effects of speckle noise. First, fixed values of $z_R$ and $z_f$ were determined from the calibration images, then the remainder of the images were analyzed using only $\mu_t$ and the product $S_0\sqrt{\mu_b}$ as free fit parameters. The 2 outlying values in each set of 12 were then removed for each of the parameters. (This was motivated by increased stability in the results, to circumvent the occasional effect of dust or an aggregated particle on local optical properties). Values of $\mu_b$ were then computed relative to that obtained from pure 2% intralipid. For dose-dependent data sets, linear least-squares fitting to Eq. (1) was employed to determine the optical constants reported in Table (1).

## 4.  Results and discussion

### 4.1.  Optical characterization of nanorods

A statistical sampling of nanorods by TEM (Fig. 3) yielded mean short and long axes of $13.7 \pm 4.5$ and $44 \pm 8$ nm, respectively, and an average aspect ratio of 3.5. In fact, only 90% of the particles were nanorods (average aspect ratio of 3.8); the remaining 10% were essentially isotropic and did not contribute appreciably to the NIR optical response. The TEM images in Fig. 3 were acquired 9 months after nanorod synthesis, providing a testament to the nanorods' long shelf life. The extinction spectrum of the nanorods revealed a longitudinal resonance (LR) peak at 784 nm and a smaller peak near 510 nm due to transverse plasmon modes. An intermediate peak lying between these two resonances is attributed to the presence of a small percentage of nanoparticles with squarish cross sections (Fig. 3). Mie-Gans calculations[26] over the size distribution of these nanorods are in accord with the unnormalized experimental data with respect to both peak positions and heights. The discrepancy in peak position is attributed to modifications in the dielectric function induced by the adsorbed sulfide and surfactants, which were not included in the model calculations. The full width at half maximum of the LR peak is 135 nm, which is likely broadened by the distribution of the nanorods' aspect ratios.

The measured albedo $a = \mu_s/\mu_t$ of the nanorods solution at 768 nm using DIS was 0.22 with a random error of 0.05 and possible systematic error of 0.05.[34] In comparison, Mie-Gans calculations of the albedo at 734 nm (chosen based on the spectral shift observed in Fig. 3) predict a value of 0.09. It is not clear whether the discrepancy is due to the aforementioned limitations in the model, or perhaps systematic errors inherent to the DIS albedo measurement. Nevertheless, it is apparent that the extinction by these nanorods is primarily due to absorption.
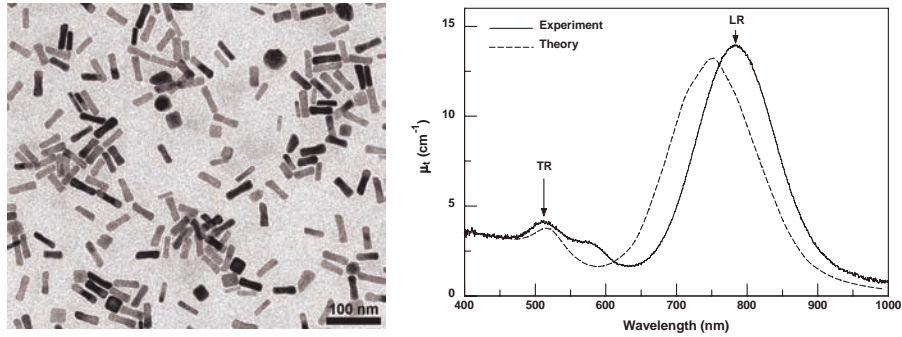
Fig. 3. Left: TEM image of SPR nanorods. Right: Extinction spectra of nanorods in water at 136 ppm. TR, transverse resonance; LR, longitudinal resonance. An intermediate peak is produced by a small percentage of non-rodlike nanoparticles.

The nanorods' extinction cross section $C_t$ at 780 nm was estimated to be $1.3 \times 10^{-15}$ m$^2$. Theoretical calculations on the optical properties of nanorods indicate that the cross section can be increased by $\sim 4$ times for a completely size monodisperse sample. In comparison, nanocages and nanoshells used in previous OCT studies were reported to have $C_t$ of $1.3 \times 10^{-14}$ m$^2$[19] and $\sim 4 \times 10^{-14}$ m$^2$[16] respectively, both at SPR wavelengths near 800 nm. We estimate that both the volume and surface area of the nanorods are 6-7 times smaller than that of the nanocages (approximating the cages as cubes), which suggests that greater dosages of nanorods might be tolerated for *in vivo* applications.[40]

### 4.2. Measuring backscattering albedo with OCT

The measured backscattering coefficient $\mu_b$, which is a portion of the total scattering coefficient $\mu_s$, is largely dependent on the numerical aperture specific to the OCT system (that is, the solid angle over which backward-directed scattered light is detected). In this application we wish to detect a change in the medium $a'$ induced by contrast agents, thus only a measure of $\mu_b$ relative to the tissue need be obtained. DIS measurements of the contrast agents' optical properties were correlated with OCT measurements to establish the physical basis for $a'$ (see Table (1)). Both the low backscattering albedo nanorods and the higher backscattering albedo silica spheres exhibit significantly smaller $a'$ relative to intralipid. For the nanorods, this is clearly due to their much smaller scattering cross section. For the silica spheres, however, the albedo measured by DIS is essentially identical to the intralipid. This discrepancy between $a$ and $a'$ can be resolved by recognizing that the silica spheres exhibit larger $g$ (more forward-scattering) than intralipid, resulting in a smaller fraction of backscattering $\mu_b$. But overall, it appears that using agents with dominant absorption such as nanorods results in a greater modification in $a'$ from tissue.

Table 1. Summary of measured optical properties of aqueous suspensions of gold nanorods (136 ppm $\approx$ 0.0007% v/v), silica spheres ($\sim$1% v/v), and intralipid (2% v/v). Values reported as mean $\pm$ standard deviation of sampled data.

|  | DIS $\mu_t$(cm$^{-1}$) | OCT $\mu_t$(cm$^{-1}$) | DIS $a = \mu_s/\mu_t$ | DIS $g = \langle \cos\theta_s \rangle$ | OCT $a' = \mu_b/\mu_t$ |
|---|---|---|---|---|---|
| Gold Nanorods | $13.6 \pm 0.6$ | $13.1 \pm 0.3$ | $0.22 \pm 0.05$ | - | $0.095 \pm 0.08$ |
| Silica Spheres | $21.7 \pm 0.2$ | $13.0 \pm 0.6$ | $0.95 \pm 0.04$ | $0.90 \pm 0.03$ | $0.5 \pm 0.2$ |
| Intralipid | $41 \pm 1$ | $35.0 \pm 0.3$ | $0.998 \pm 0.002$ | $0.53 \pm 0.02$ | 1 (definition) |

The other interesting feature of Table (1) is the mismatch between $\mu_t$ measured by the two techniques. This is partially explained by the different wavelengths used for DIS (768 nm) and OCT (centered at 810 nm); based on spectrophotometry we predict a reduction in $\mu_t$ to 87-94% for the various solutions at the longer OCT wavelength. The additional discrepancies in the silica spheres and intralipid measurements (45% and 4% in $\mu_t$ unaccounted for, respectively) is attributable to multiple-scattering which makes the OCT signal appear artificially larger at greater depths, resulting in less apparent attenuation and an underestimation of $\mu_t$. The fact that the silica spheres exhibited the most difference can be attributed to their high $g$ and thus larger amount of forward-scattering, which is associated with a greater amount of multiply-scattered light being detected.[41]

The results above suggest that greater accuracy in predicting optical constants might be achieved using a multiple-scattering model for OCT. However, this is not an absolute requirement for contrast imaging, as it is only necessary to measure relative changes in optical properties due to the contrast agents. Thus, we show in the following studies that the changes in $\mu_t$ and $\mu_b$ are linear with respect to $\rho_{tiss}$ and $\rho_{ca}$, allowing $\rho_{ca}$ to be extracted using Eq.(1).

Figure 4 illustrates the ability to fit depth-dependent OCT data over more than one decade of tissue phantom concentrations, verifying the linearity of $\mu_b$ and $\mu_t$ over a biologically relevant range of intralipid concentrations. In the center panel of the Fig. 4 we see that the best-fit lines, which exclude the region immediately below the top surface, match the data curves extremely well except for the most concentrated sample (4%) for which multiple-scattering becomes significant. The gentle curve in the resulting $\mu_t$ values (top right panel of Fig. 4) is expected for higher volume fractions of intralipid which slightly deviate from the independent scattering approximation.[36] Most importantly, the measurement of $a'$ is essentially constant ($\pm 6\%$) over the 0.5-3% concentration range, which suggests that large fluctuations in tissue density will not elicit significant variations in $a'$. Based on previous work we expect the 2% intralipid tissue phantoms used in the following experiments will mimic human skin,[33], however, it remains to be shown whether the backscattering albedo is constant within various types of biological tissues.
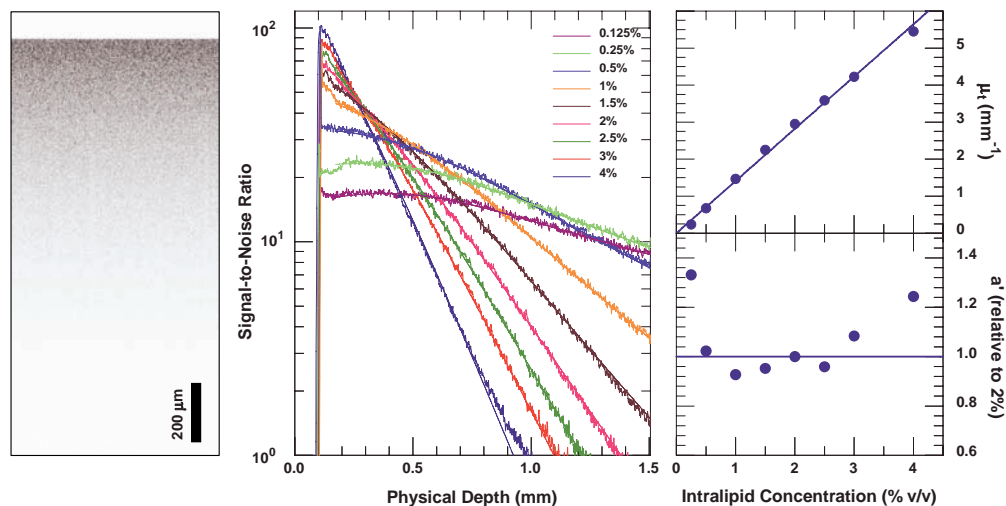


Fig. 4. OCT imaging while varying the concentration of the tissue phantom. Left: Example M-mode OCT image. Middle: Depth-dependent OCT data are plotted with their best-fit lines according to Eq.(6). Right: The extracted extinction coefficient $\mu_t$ and backscattering albedo $a'$ are plotted versus the tissue phantom concentration.

### 4.3. Differential backscattering albedo detection with OCT

The dose-dependent changes in the OCT-derived optical constants for low backscattering albedo nanorods and higher backscattering albedo silica spheres embedded in a homogeneous tissue phantom with fixed $\rho_{tiss}$ (2% intralipid) are displayed in Fig. 5. The contrast agent concentrations were chosen to produce the same range of optical extinction. We find the dose-dependent response to be linear in $\mu_b$ and $\mu_t$ according to Eq.(1). As expected, the modification of $a'$ is larger using the low backscattering albedo nanorods. The fact that the silica spheres also reduce $a'$ is due to their higher forward-scattering ($g$) relative to the tissue phantom medium (see Table 1). The responses appear to be well-described by the independent scattering approximation of Eq.(1). The standard deviation from theory in $\mu_t$ and $a'$ are respectively 0.02 mm$^{-1}$ and 0.01 for nanorods, and 0.06 mm$^{-1}$ and 0.02 for silica spheres. The higher variation in the silica spheres values can be ascribed to unaccountable effects such as multiple-scattering. Based on this study, the measurement error in $a'$ obtained at a constant tissue density is expected to be between 1 and 2%, which is less than observed with variable tissue phantom concentrations in the previous subsection.
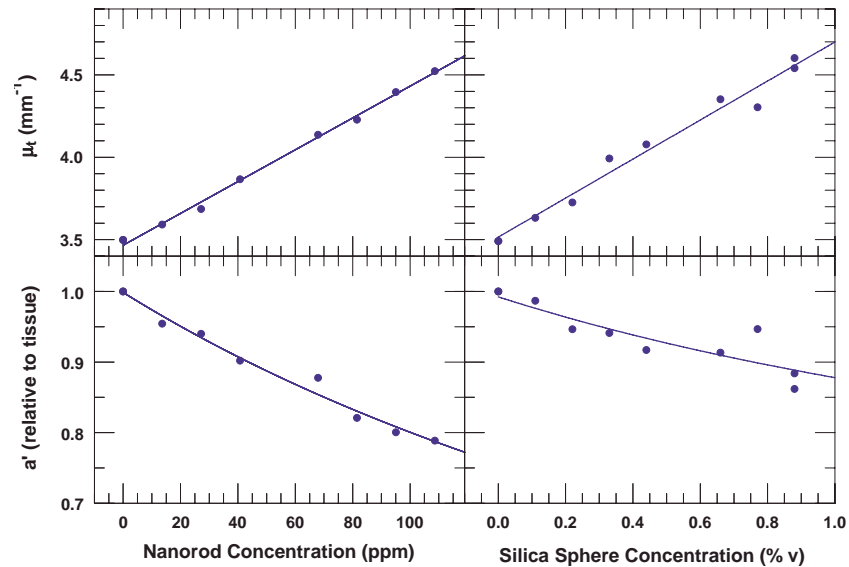


Fig. 5. Dose-dependent changes in $\mu_t$ (top row) and $a'$ (bottom row) while mixing gold nanorods (left column) and silica spheres (right column) with 2% intralipid, as measured from OCT images. Best-fit lines according to Eq.(1) are plotted. Scales are uniform along rows and columns to aid in comparison.

The advantages of using backscattering albedo-based contrast are most evident when attempting to discriminate contrast agents in a sample with randomly fluctuating density $\rho_{tiss}$. For example, if an uncertainty $\sigma_{\rho_{tiss}}$ of 20% is assumed for the 2% intralipid, the amount of nanorods needed to change $\mu_t$ by two standard deviations for extinction-based contrast would be 145 ppm. This is much greater than what is needed for contrast based on $a'$, which we estimate to be in the range of 8-50 ppm for standard deviations in $a'$ between 1% and 6%.

To demonstrate this, we examined several homogeneous tissue phantom samples with randomly chosen $\rho_{tiss}$, half containing nanorods (82 ppm) and half without (see Fig. 6). Looking along the horizontal, $\mu_t$ axis we see that it is not possible to distinguish tissue phantoms containing nanorods from the control samples based on this parameter alone, because the added

nanorods did not significantly raise $\mu_t$. In comparison, the two groups appear to be well-separated with respect to $a'$. The apparent positive slope in $a'$ versus $\mu_t$ for the tissue phantoms with nanorods is partially explained by the fact that the nanorods' concentration was fixed, so that increasing intralipid concentration resulted in both increased $a'$ and $\mu_t$. In addition, it should also be noted that the $\rho_{tiss}$ of some samples may lie above the linear response range (cf. Fig. 4), resulting in an overestimate of $a'$ at high concentrations. This systematic error might be reduced by using a simple correction factor or employing a model which takes multiple-scattering effects into account. However, the drawback to incorporating multiple-scattering models is the need to fit the anisotropy factor, $g$,[29] which adds another degree of freedom.
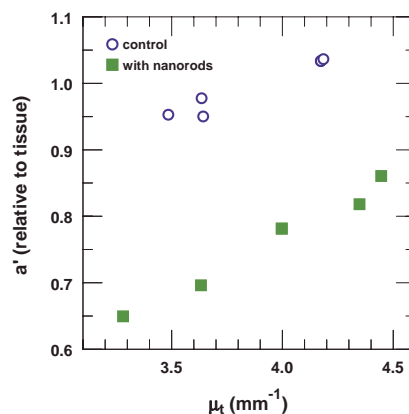


Fig. 6. Discrimination of nanorods within tissue phantoms of randomly chosen concentration, using backscattering albedo-based OCT contrast. Intralipid samples ($2 \pm 0.4\%$) without nanorods (open circles) are distinguished from those containing nanorods (82 ppm, filled squares) by the parameter $a'$.

The prior knowledge of the tissue and contrast agent optical properties were then used to calculate $\rho_{ca}$ for each of the data points in Fig. 6 according to Eq.(2). The control group yielded a mean value of $3 \pm 14$ ppm (statistically zero), whereas the group containing nanorods yielded a mean $\rho_{ca}$ of $104 \pm 27$ ppm, which is in agreement with the actual nanorod concentration of 82 ppm. Although a larger sampling population would yield a more precise estimate of $\sigma_{\rho_{ca}}$, we believe that the standard deviation of this measurement ($\sim 30$ ppm) represents the concentration threshold for detecting nanorods in a tissue-like medium with a 20% uncertainty in concentration.

## 5. Conclusions and future outlook

We have identified a new contrast mechanism for OCT based on the backscattering albedo $a' = \mu_b/\mu_t$. This form of contrast is particularly well-suited for detecting exogenous agents with low backscattering albedo in highly scattering tissues. In this study, we have found plasmon-resonant nanorods to be excellent OCT contrast agents. The nanorods' low backscattering albedo, which is a direct consequence of particle size ($< 50$ nm in length), permits them to be detected within an intralipid tissue phantom with uncertain concentration by measuring changes in $a'$, at concentrations where changes in extinction were insignificant. The tunability of nanorod resonances throughout the NIR wavelength range is particularly appealing, as it may be further exploited by spectroscopic OCT. Improvements in the nanorods' spectral linewidth may be achieved by modifications in the seeded growth conditions. It has recently been shown that the quality of the nanoparticle seed strongly influences the outcome

of anisotropic growth, and can result in NIR-resonant nanostructures with linewidths well below 100 nm.[42] There are currently limitations to the expected sensitivity with which absorption profiles can be detected using SOCT.[43] However, by coupling the backscattering albedo-based detection scheme with spectroscopic techniques, it may be possible to combine the advantages of both techniques for heightened sensitivity and imaging specificity.

We also found that it is possible to detect changes in $a'$ from silica spheres with similar albedo ($\mu_s/\mu_t$) but different angular scattering property ($g$) relative to the tissue. Although these changes were smaller than those provided by the nanorods, it suggests the intriguing future possibility of differentiating endogenous scatterer types using $a'$. Because human tissues exhibit primarily forward-scattering behavior,[32] we anticipate that $a'$ can be modified by use of either a backscattering agent which raises $a'$, or an absorbing agent which lowers it. Although resonantly backscattering agents have been explored as potential contrast agents[8, 18], generally they have been limited to the submicron- to micron-size range. We also found that experiments using scattering silica spheres exhibited larger variance in $a'$ than the absorbing nanorods. It appears that the use of absorbing nanorods minimized the undesired effects of multiple-scattering, allowing for increased accuracy in the measurement of $a'$.

Currently, our estimated threshold for nanorods detection in a tissue sample with uncertainty in its concentration ($\sim 3.5 \pm 0.7$ mm$^{-1}$) is 30 ppm $\approx 0.00015\%$ v/v in an aqueous medium, based on measurements of nanorods added to intralipid. Recent studies have indicated that gold nanoparticles and nanorods with appropriate surface coatings do not exhibit cytotoxicity at this concentration.[12, 13, 14] We estimate this concentration theshold corresponds to a nanorod number density of $2.7 \times 10^{11}$cm$^3$. This may be relevant for cell surface receptor targeting, because for an average cell volume equivalent to a 10 $\mu$m diamter sphere, this threshold corresponds to a minimum of 140 nanorods per cell. NIR-resonant nanoparticles are also known to be highly efficient at converting light energy into heat,[44] with application for inflicting photothermal tissue damage.[45, 46, 47] It is not yet known whether the moderate light intensities and low exposure times used for OCT imaging are sufficient to cause incidental damage to the surrounding tissue. However, further improvements in the sensitivity of backscattering albedo-based contrast will lower the light exposure and nanorod dosage requirements for OCT detection and minimize any negative consequences for nanorod-induced heating.

Methods for biomolecular conjugation of nanorod surfaces can provide chemical specificity to cellular receptors,[48, 49, 46] enabling molecular OCT imaging using the backscattering albedo-based contrast method of this study. Furthermore, the application of highly absorbing, ligand-functionalized nanorods for site-specific hyperthermia[46, 47] creates the possibility of combining OCT imaging and photothermal therapy into an integrated platform. Clearly, the ability to provide molecular imaging using OCT will greatly aid in developing nanoparticle-based and image-guided therapies for the future.

Further work is also needed to provide depth-resolved discrimination of nanorods, and to demonstrate imaging in heterogeneous tissues, toward the goal of providing calibrated concentration maps. We also anticipate a tradeoff between the imaging resolution and the amount of speckle-averaging necessary to achieve the desired sensitivity (by averaging over area, volume, and/or time). Ultimately, these parameters will determine the optimal balance between the OCT signal intensity and a tolerable contrast agent dosage.